Optical Modulation of MoTe₂/Ferroelectric Heterostructure via Interface Doping

Yuqing Zhou, Chao Yang, Xingke Fu, Yadong Liu, Yulin Yang, Yongyi Wu, Chen Ge, Tai Min, Kaiyang Zeng,* and Tao Li*

Read Online

ACCESS | Metrics & More | Article Recommendations | Supporting Information

ABSTRACT: Optical modulation through interface doping offers a convenient and efficient way to control ferroelectric polarization, thereby advancing the utilization of ferroelectric heterostructures in nanoelectronic and optoelectronic devices. In this work, we fabricated heterostructures of MoTe₂/BaTiO₃/La₀.₇Sr₀.₃MnO₃ (MoTe₂/BTO/LSMO) and demonstrated opposite ultraviolet (UV) light-induced polarization switching behaviors depending on the varied thicknesses of MoTe₂. The thickness-dependent band structure of MoTe₂ film results in interface doping with opposite polarity in the respective heterostructures. The polarization field of BTO interacts with the interface charges, and an enhanced effective built-in field (E_{bi}) can trigger the transfer of massive UV light-induced carriers in both MoTe₂ and BTO films. As a result, the interplay among the contact field of MoTe₂/BTO, the polarization field, and the optically excited carriers

determines the UV light-induced polarization switching behavior of the heterostructures. In addition, the electric transport characteristics of MoTe₂/BTO/LSMO heterostructures reveal the interface barrier height and E_{bi} under opposite polarization states, as well as the presence of inherent in-gap trap states in MoTe₂ and BTO films. These findings represent a further step toward achieving multifield modulation of the ferroelectric polarization and promote the potential applications in optoelectronic, logic, memory, and synaptic ferroelectric devices.

KEYWORDS: 2D TMD, MoTe₂/ferroelectric heterostructure, domain modulation, interface doping, optoelectronic
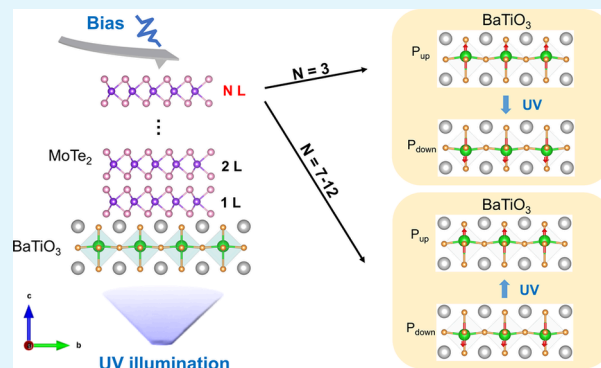
1. INTRODUCTION

Ferroelectric materials possess switchable spontaneous polarizations below a critical temperature. An electric field is the most common method to switch polarization, while other external stimuli, such as stress field,[1−5] chemical doping,[6,7] and light,[8−10] also have been reported to modulate ferroelectric polarization. Among those methods, optical modulation is one of the most convenient and flexible ways to interact with the polarization order. Their interaction can be classified as a thermoelectric effect induced by high-intensity laser illumination,[11,12] bulk photovoltaic effect owing to the noncentrosymmetric crystal structure,[13,14] and interfacial photovoltaic effect induced by interface doping.[8,15−18] Optical-induced polarization switching based on the thermoelectric effect is always irreversible and destructive. A former research[13] achieved reversible control of ferroelectric polarization based on the bulk photovoltaic effect, while that occurs only with certain crystal orientation or light polarization. The interface photovoltaic effect is a nondestructive and universal method for all two-dimensional (2D) heterostructures, which can be modulated by the number of atomic layers, electrostatic doping, surface modulation, and band alignment.[19−21] Some

studies investigated interface photovoltaic effects in ferroelectric heterostructures and exploited their applications in optoelectronic memories,[14,15,22−25] optoelectronic detectors,[26] neuromorphic devices,[16,27,28] and even single-chip microprocessors,[29] indicating the widespread applications in nanoelectronic and optoelectronic devices. Nevertheless, the interface photovoltaic effects of many ferroelectric heterostructures with various band alignment conditions still have much room to be explored.

2D van der Waals transition metal dichalcogenides (TMDs) have been considered promising semiconductors for next-generation nanodevices mainly because of their thickness-dependent band structure and intriguing electronic and optoelectronic features. When TMDs form heterostructures with ferroelectric films, a contact field is induced at the
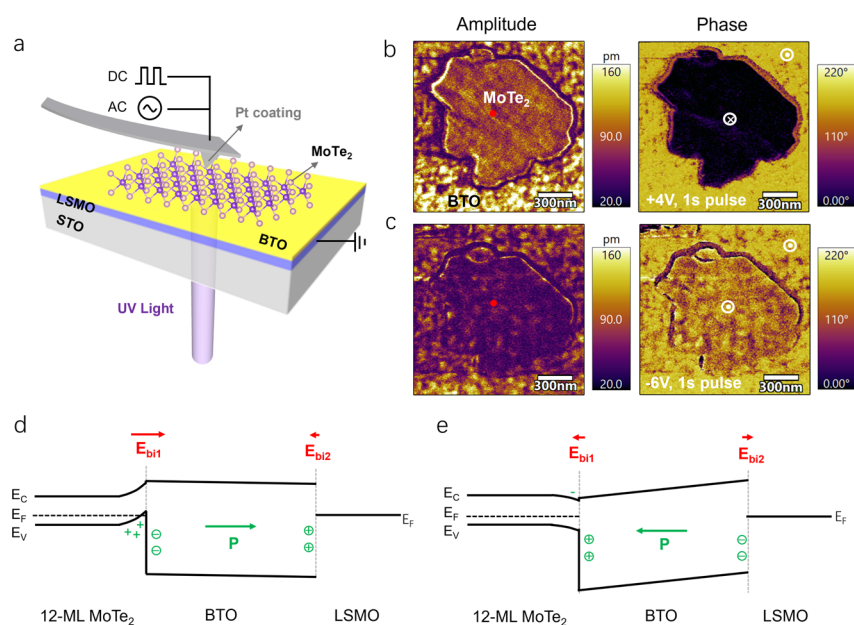
Figure 1. Electrically induced ferroelectric polarization switching on a MoTe$_2$/BTO/LSMO heterostructure. (a) Schematic of the PFM measurement setup integrated with UV light illumination. PFM amplitude and phase images after switching the polarization of MoTe$_2$/BTO to the (b) P_{down} state and (c) P_{up} state by exerting an electric pulse of (+4 V, 1 s) and (−6 V, 1 s), respectively, on the surface of the MoTe$_2$ film. Schematics show the band alignment of MoTe$_2$/BTO/LSMO heterostructures after switching the polarization of BTO to (d) P_{down} and (e) P_{up}. E_C, E_F, and E_V represent the conduction band edge, Fermi level, and valence band edge, respectively. E_{bi1} and E_{bi2} are the total built-in fields near MoTe$_2$/BTO and BTO/LSMO interface, respectively. Bare green "+" and "−" signs indicate the mobile screening charges near the MoTe$_2$/BTO interface, while circled green "+" and "−" indicate the bound charges inside the BTO film.

interface to match their work functions. Additionally, the polarization field of ferroelectric films attracts mobile charges of TMDs accumulated at the TMDs/ferroelectric interface to screen the bound charge, which stabilizes the polarization and leads to a nonvolatile interface electrostatic doping of TMDs.[30−35] Moreover, light-induced carriers also alter the density of screening charges and can even switch the polarity of the interface doping under an appropriate electronic band offset. Based on the polarization- and light-dependent interface doping, studies achieved optical-induced polarization switching from P_{up} to P_{down} states based on the MoS$_2$/BaTiO$_3$ heterostructure[8] and recently realized the optoelectronic synapse and neuromorphic vision sensor based on its electrical and optical tuning memory functions.[16] In the study,[8] the optical-induced polarization switching occurred when major carriers in MoS$_2$ were depleted; however, only unidirectional optical-induced polarization switching was achieved.

In this work, we use bipolar MoTe$_2$ with different thicknesses as the top electrode on ferroelectric thin films, the polarity of which can be easily switched by interface doping, and its band structure can be modulated by thickness. Opposite optical-induced polarization switching has been realized in a MoTe$_2$/BaTiO$_3$/La$_{0.7}$Sr$_{0.3}$MnO$_3$ (MoTe$_2$/BTO/LSMO) heterostructure with different MoTe$_2$ thicknesses. Specifically, UV-induced polarization switching from P_{down} to P_{up} states is achieved using MoTe$_2$ films with a thickness range of about 5−8 nm, while the switching from P_{up} to P_{down} states is observed when the thickness of MoTe$_2$ is reduced to about 2.15 nm. The thickness-dependent band structure of MoTe$_2$ can result in an opposite interface contact field when the heterostructure is formed. Additionally, the ferroelectric polarization field has the opposite effect on interface doping (i.e., to enhance or weaken the effective E_{bi}). Only the enhanced effective E_{bi} motivates the transfer of the UV light-

induced carriers in both MoTe$_2$ and BTO films, enabling the change of the polarity of interface doping and resulting in the switching of the polarization of the BTO film. Furthermore, lateral and vertical electric transport characteristics of the MoTe$_2$/BTO/LSMO heterostructures indicate that in-gap trap states inherently exist in MoTe$_2$ and BTO films, which may decelerate the process of UV-induced polarization switching. These results provide more possibilities for optical modulation of polarization orientation, and interface doping can be an appropriate and universal method for all semiconductor/ferroelectric heterostructures to modulate the performance of electronic and optoelectronic devices.

2. RESULTS AND DISCUSSION

To switch the polarization orientation of the BTO film to the P_{down} (or P_{up}) state electrically, we grounded the bottom LSMO electrode and applied a positive (or negative) bias on the top MoTe$_2$ layer through a conductive probe. When performing in situ photoelectric measurements, UV light was applied through the sample bottom using an illuminating system integrated with a piezoresponse force microscope (PFM). The schematic of PFM measurement on a MoTe$_2$/BTO/LSMO heterostructure is shown in Figure 1a. The electrical-induced polarization switching of the heterostructure is shown in Figure 1b,c, where PFM amplitude represents the piezoresponse strength and ∼180° PFM phase contrast manifests the opposite polarization orientation of the ferroelectric layer. The electric pulse-induced reversible polarization switching of the entire area of MoTe$_2$/BTO/LSMO heterostructure suggests a bipolar transport characteristic of the MoTe$_2$ film, in which both sufficient holes and electrons can be accumulated at the MoTe$_2$/BTO interface to stabilize the polarization of the BTO film. The ferroelectric hysteresis loops measured on the heterostructure are shown in Figure S1,
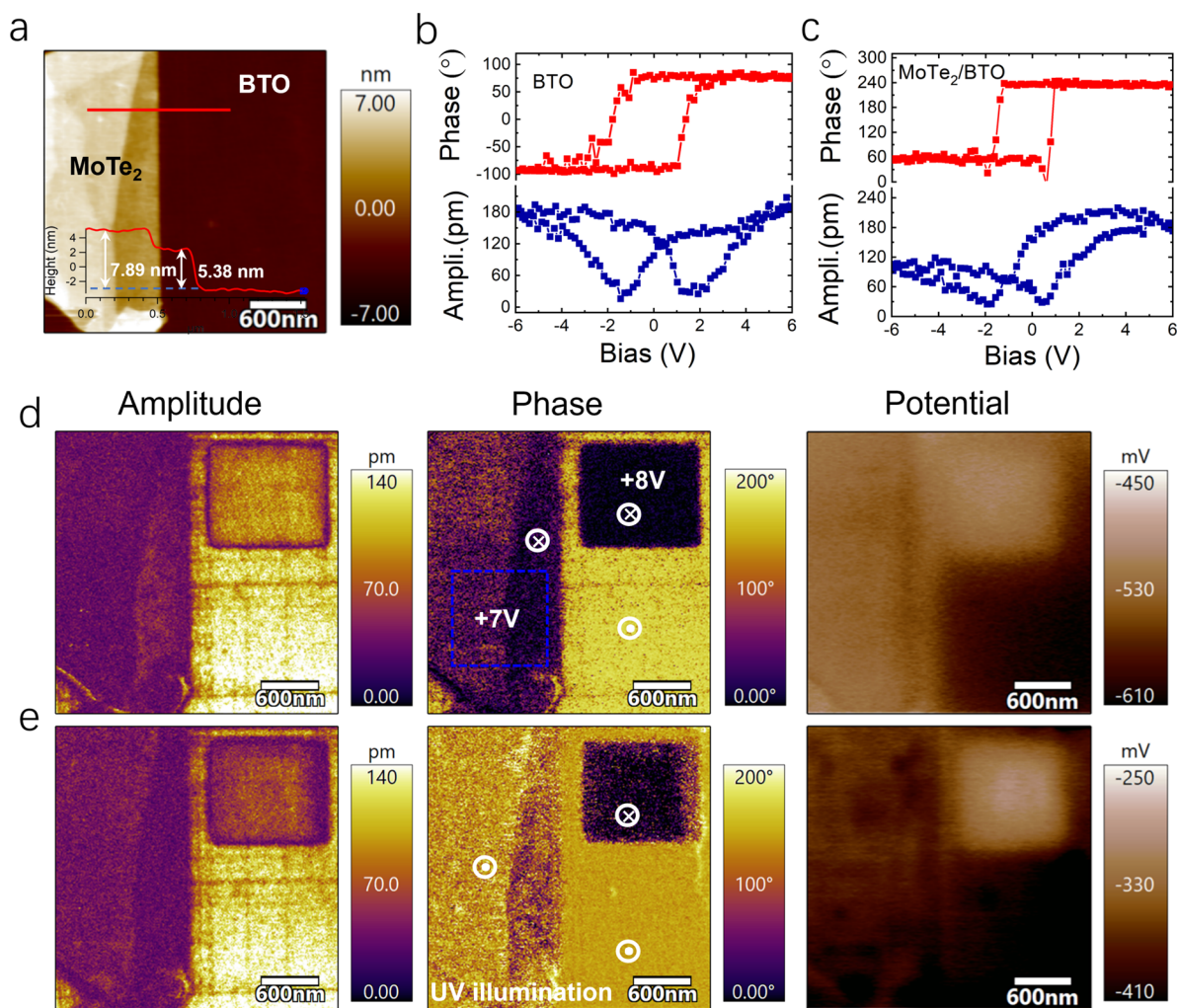
Figure 2. UV light-induced ferroelectric polarization switching from P_{down} to P_{up} states on a MoTe$_2$/BTO/LSMO heterostructure. (a) Morphology of the heterostructure. The inset is the height profile along the red line indicating that MoTe$_2$ is about 12-ML. Phase and amplitude hysteresis loops were obtained at (b) the bare BTO/LSMO region and (c) the MoTe$_2$/BTO/LSMO regions. (d) PFM and KPFM images after the polarization switching to P_{down} by +7 V bias scanning within the blue dotted square. A +8 V DC scanning was conducted on the bare BTO/LSMO region (dark square in the phase image) to work as a reference state with P_{down} state. (e) PFM and KPFM images of the heterostructure after applying 20 min of UV illumination.

where the loops measured on bare BTO surface and MoTe$_2$/BTO showed the opposite imprints and asymmetric amplitude responses. In the MoTe$_2$/BTO/LSMO heterostructure, the space charges and injected charges under strong electric fields tend to gather at the MoTe$_2$/BTO interface and an E_{bi} pointing toward the BTO/LSMO interface can be induced.

To understand the interface conditions in the MoTe$_2$/BTO/LSMO heterostructure, we systematically studied the band structure of MoTe$_2$, BTO, and LSMO before and after their contacts. When forming a heterostructure, charges can transfer from MoTe$_2$ to BTO, and from BTO to LSMO due to band alignment, leading to $-E_{bi}$ (along the P_{down} direction) at the MoTe$_2$/BTO and BTO/LSMO interfaces. This E_{bi} is contributed by the contact field (as shown in Figure S2a,b) and the excitation state band diagrams upon applying a positive or negative bias on the surface of MoTe$_2$ film are also exhibited in Figure S2c,d. This band structure modulation induced by an external electric field is specifically illustrated in Section S2. When the polarization of BTO has been switched to the P_{down} state after applying a positive bias on the surface of MoTe$_2$, due to the same direction between the contact field and the

external electric field, the effective E_{bi} and band bending at the MoTe$_2$/BTO interface is enhanced and massive holes accumulated at the interface that stabilized the P_{down} state of the BTO film (Figure 1d). In contrast, when the polarization of BTO has been switched to the P_{up} state by applying a negative bias on the surface of the MoTe$_2$, the external electric field possesses an opposite direction compared with the direction of the contact field. Therefore, the effective E_{bi} and band bending decrease and can even be switched to an opposite direction. In this case, electrons can transfer and gather at the MoTe$_2$/BTO interface under the effect of an external bias, which can act as screening charges to switch and stabilize the P_{up} state of the BTO film (Figure 1e). Based on the band alignment in Figure 1, we expect that MoTe$_2$, acting as a good top electrode, can transfer sufficient carriers into the MoTe$_2$/BTO interface to mutually switch and stabilize the opposite polarizations of the BTO film. Hence, both p-type and n-type interface doping of MoTe$_2$ can be realized when switching the polarization of BTO film to the P_{down} or P_{up} state, which implies that opposite effective E_{bi} can be induced at the MoTe$_2$/BTO and BTO/LSMO interfaces by the polarization field.
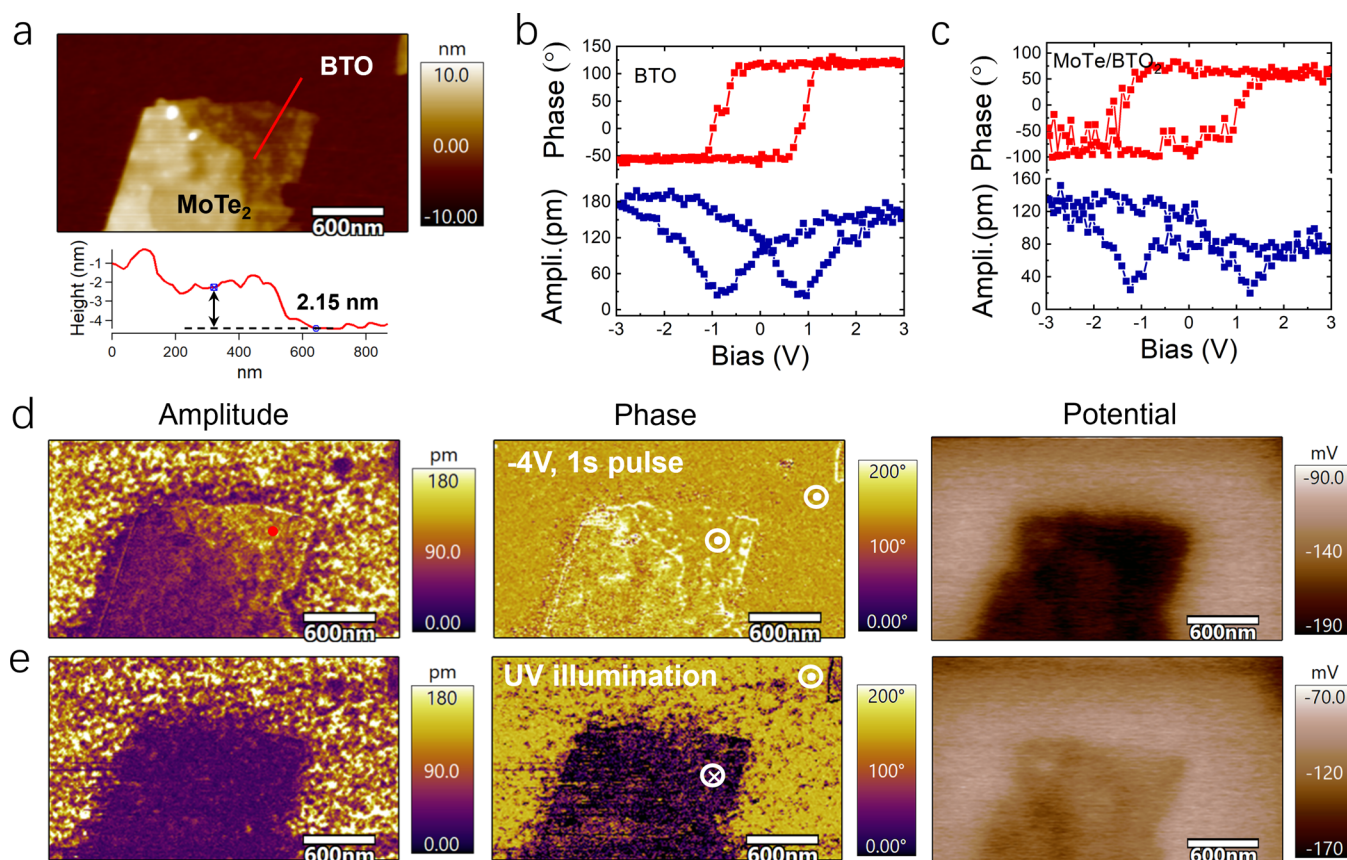
Figure 3. UV light-induced ferroelectric polarization switching from P_{up} to P_{down} states on the 3-ML MoTe$_2$/BTO/LSMO heterostructure. (a) Morphology of the heterostructure. Inset is the height profile along the red line, indicating that the thinnest MoTe$_2$ is 2.15 nm thick. Phase and amplitude hysteresis loops were obtained at the (b) bare BTO/LSMO region and (c) MoTe/BTO/LSMO region. (d) PFM and KPFM images when the polarization orientation of the heterostructure was switched to the P_{up} state by applying a (−4 V, 1 s) pulse bias at the position marked by the red dot. (e) PFM and KPFM images of the heterostructure after applying UV illumination for 19 min.

Subsequently, we investigated the light effect exerted on the MoTe$_2$/BTO/LSMO heterostructure. Since crystal defects significantly impact the transport phenomena of the photo-induced carriers, we conducted X-ray diffraction (XRD) characterization for the BTO film and MoTe$_2$ crystal, as well as the Raman spectrum on the MoTe$_2$/BTO/LSMO heterostructures. The results confirm that the films are high-quality single-crystals and the crystallographic directions of BTO and 2H-MoTe$_2$ are along <100>$_{pc}$ and <001>, respectively (Figures S3a and S4). Moreover, to select a suitable wavelength of light to illuminate the heterostructure, we conducted photoluminescence (PL) measurements of the BTO film and MoTe$_2$ crystal and found that the band gaps of the BTO film and MoTe$_2$ crystal are 3.70 and 1.11 eV, respectively (Figure S3b). Therefore, we selected blue light (450 nm wavelength, ∼2.76 eV) and UV light (continuous UV light with a peak at 250 nm wavelength, ∼4.96 eV) to study photoinduced polarization switching behavior in the MoTe$_2$/BTO/LSMO heterostructure.

Figure 2a shows the morphology image of a MoTe$_2$/BTO/LSMO heterostructure, with the line profile showing a MoTe$_2$ thickness of ∼7.89 nm (12-ML) in the inset. The hysteresis loops obtained from bare BTO/LSMO and MoTe$_2$/BTO/LSMO regions are shown in Figure 2b,c, with the latter showing a strong negative imprint. When 450 nm light is illuminated on this sample, only carriers in MoTe$_2$ can be excited and the light needs to couple with an electric bias to

switch the polarization of BTO (Figures S5 and S6). On the contrary, when UV light is used to excite the sample, we observed pure light-induced polarization switching from P_{down} to P_{up} in the MoTe$_2$/BTO/LSMO heterostructure, as shown in Figure 2d,e. Here, we first switched the polarization orientation of the MoTe$_2$/BTO/LSMO heterostructure to the P_{down} state by applying +7 V bias scanning within the blue dotted square in Figure 2d. Then, a UV light was illuminated from the backside of the sample and the PFM phase image showed that the polarization of BTO film was switched to the P_{up} state after 20 min of UV illumination (Figure 2e). The entire switching process under different illumination durations is illustrated in Figure S7. To further confirm the UV-induced polarization switching behavior, we conducted Kelvin probe force microscopy (KPFM) to measure the surface potential distribution of the heterostructure. If UV light-induced carriers are not stimulated or trapped by some defects, they will not transport under an E_{bi} of the heterostructure, and thus the surface potential will remain constant. The KPFM images in Figure 2d,e manifest a potential decrease of the MoTe$_2$/BTO/LSMO region after UV illumination and corroborate the UV-induced polarization switching behavior of the heterostructure. Compared to the MoS$_2$/BTO heterostructure, the polarization of which is switched from P_{up} to P_{down} under UV illumination,[8] in the MoTe$_2$/BTO heterostructure, UV illumination caused an opposite direction of polarization switching from P_{down} to P_{up} as described above.
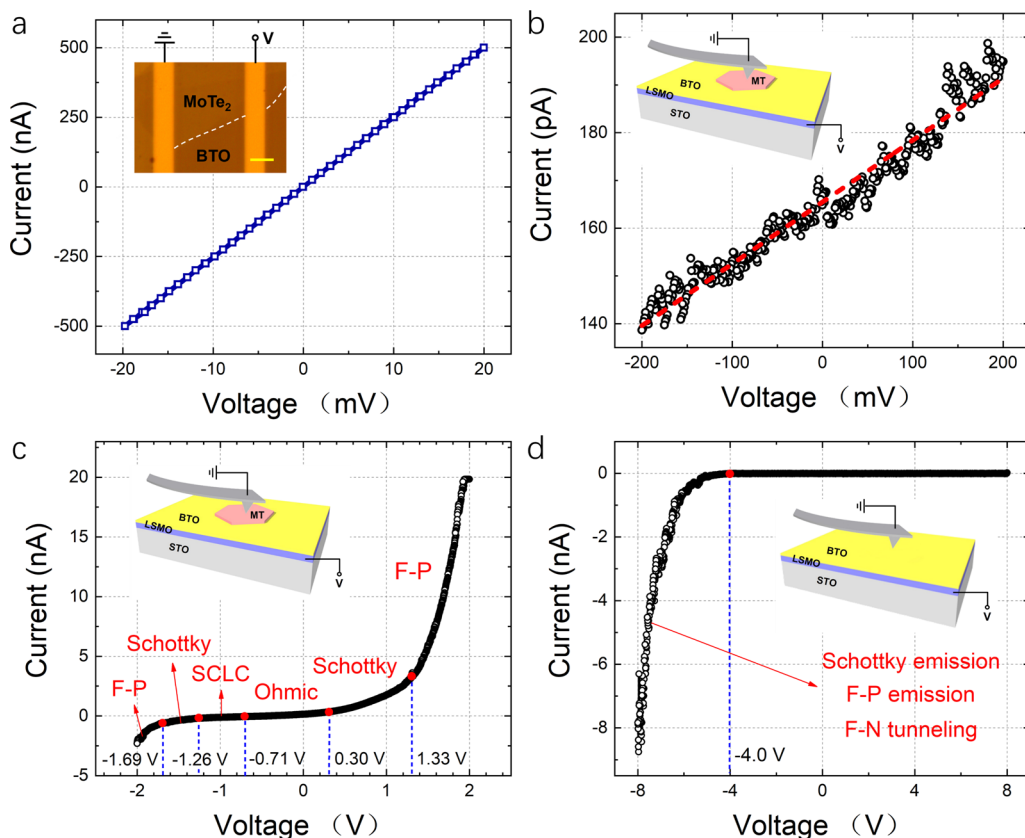
Figure 4. Electronic transport characteristic curves of MoTe$_2$/BTO/LSMO and BTO/LSMO heterostructures. (a) In-plane I_{ds}−V_{ds} curve measured on the surface of the MoTe$_2$/BTO/LSMO heterostructure, where 0 V bias was applied to the LSMO gate electrode. The inset is the morphology of the test region where the thickness of MoTe$_2$ is 7.04 nm and the scale bar is 10 μm. (b) Vertical I−V curve of the MoTe$_2$/BTO/LSMO heterostructure under the voltage range of $\pm$200 mV, where the red dotted fitting line indicates Ohmic conduction dominates in this voltage range. The inset is the schematics of the CAFM test, where the SPM probe is grounded and the voltage is applied to the bottom LSMO electrode. The thickness of MoTe$_2$ in this heterostructure is 4.49 nm. (c) Vertical I−V curve of MoTe$_2$/BTO/LSMO heterostructure under the voltage range of $\pm$2 V, where different conduction mechanisms are labeled and separated by red spots. (d) Vertical I−V curve of the bare BTO/LSMO heterostructure under the voltage range of $\pm$8 V.

We also conducted the same experimental measurements on another MoTe$_2$/BTO/LSMO heterostructure with much thinner MoTe$_2$ (~2.15 nm, 3-ML) as the top electrode (Figure 3a). The hysteresis loop obtained at the MoTe$_2$/LSMO region in this sample (Figure 3c) exhibits nearly zero imprint value compared with the loop shown in Figure 2c, which indicates the existence of a potentially opposite built-in field. In this heterostructure, when we applied a positive bias to the MoTe$_2$ to switch the polarization direction to P_{down} and then illuminated a UV light on the sample, we did not observe the polarization switching (Figure S8) as described in the heterostructure with thicker MoTe$_2$ (Figure 2). Nevertheless, when we applied a negative electric pulse on MoTe$_2$ to switch the polarization of BTO to P_{up} first (Figure 3d), the polarization of BTO film was switched to P_{down} after 19 min of UV illumination (Figure 3e). Here, we observed an opposite UV light-induced polarization switching behavior from the P_{up} to P_{down} states by using a thinner MoTe$_2$ film. Correspondingly, the KPFM images (Figure 3d,e) clearly revealed the UV light-induced surface potential enhancement of the MoTe$_2$/BTO/LSMO heterostructure when the polarization was switched from P_{up} to P_{down}. To further investigate the effect of MoTe$_2$ thickness, we conducted PFM and KPFM measurements on the MoTe$_2$/BTO heterostructure with the thickness of MoTe$_2$ at 3.22 nm. The results show that the

polarization orientation is not switched either way after 18 min of UV illumination, which indicates that both UV light-induced polarization switching is not observed with this MoTe$_2$ thickness (Figure S9).

The band alignments of MoTe$_2$/BTO/LSMO heterostructures with 3-ML MoTe$_2$ under different conditions are illustrated in Figure S10. In comparison, the opposite electron transfer direction can be generated due to the different band alignments between 3-ML and 12-ML MoTe$_2$ with BTO. Therefore, an opposite contact field is generated along the P_{up} direction and promotes electron accumulation at the MoTe$_2$/BTO interface, which is also corroborated by the imprint behavior of hysteresis loop measurements (Figure 3c). As the contact field is along the P_{up} direction, stronger band bending and enhanced effective E_{bi} is present at the MoTe$_2$ (3-ML)/BTO interface when a negative bias (V_-) is exerted on the MoTe$_2$ film to switch the polarization to the P_{up} state (Figure S10d,f). Conversely, a positive bias (V_+) applied to MoTe$_2$ film results in a weakened effective E_{bi} due to the opposite direction between the contact field and polarization field (Figure S10c,e).

To gain further insight into the electronic property of the MoTe$_2$/BTO/LSMO heterostructure, we conducted lateral and vertical electrical measurements. It is a common practice to estimate the polarity of a semiconductor by measuring the
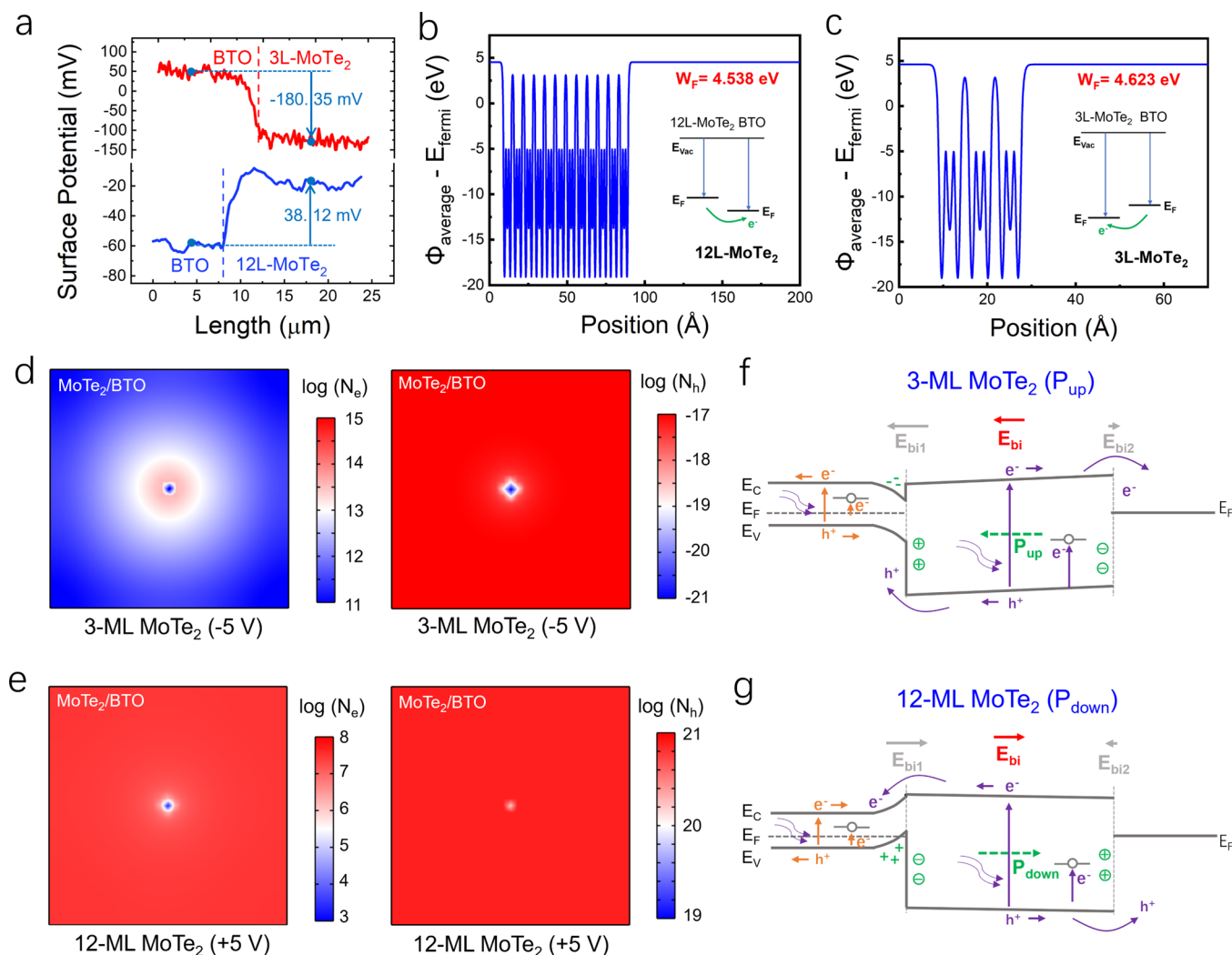
Figure 5. Mechanisms of UV light-induced opposite polarization switching of MoTe$_2$/BTO/LSMO heterostructure with MoTe$_2$ of different thicknesses. (a) Line profiles of surface potential of 3-ML MoTe$_2$/BTO and 12-ML MoTe$_2$/BTO. Calculated work functions of (b) 3-ML and (c) 12-ML MoTe$_2$ by first-principles calculations, where the inset are schematics of Fermi level alignments between MoTe$_2$ and BTO. (d) Electron concentration (left image) and hole concentration (right image) simulated by COMSOL Multiphysics at the 3-ML MoTe$_2$/BTO interface when −5 V$_{dc}$ was applied to the conductive tip to switch the polarization of BTO to the P_{up} state. (e) 12-ML MoTe$_2$/BTO interface when +5 V$_{dc}$ was applied to the conductive tip to switch the polarization BTO to the P_{down} state. Schematics of the UV-illuminated band structure of (f) 3-ML MoTe$_2$/BTO/LSMO heterostructures when the polarization of BTO is electrically switched to P_{up} and (g) 12-ML MoTe$_2$/BTO/LSMO heterostructure when the polarization of BTO is electrically switched to P_{down}. The E_{bi} here indicates the effective built-in field in the BTO film. The orange and purple e$^-$ and h$^+$ indicate UV light-induced carriers in the MoTe$_2$ and BTO film, respectively. The images indicate the transfer characteristics of these optically induced carriers under effective E_{bi}. The gray circles with a line section schematically illustrate the in-gap trap states.

transfer characteristic curves in the form of a field effect transistor (FET). We fabricated two Au/Ti electrodes on the surface of the MoTe$_2$/BTO/LSMO heterostructure as the source and drain electrodes, and LSMO film serves as the bottom gate electrode. As shown in Figure 4a, the current–voltage (I_{ds}–V_{ds}) curve under 0 V gate bias shows a perfect linear characteristic, which indicates ohmic contact and good in-plane ambipolar conductivity of the MoTe$_2$ flake, whose resistance is about 40 kΩ. This characteristic of I_{ds}–V_{ds} curve implies that many unintentional dopants and in-gap states may exist in the MoTe$_2$ film. Many other works[36−38] also reported that the exfoliated MoTe$_2$ film with several nanometer thicknesses possesses ambipolar transport behavior. The polarity of MoTe$_2$ was sensitive to the in-gap trap states induced by intrinsic Te defects[37,39] and the interface trap state

caused by the adsorption/desorption of polar molecules and contaminants,[40] which also apply to our MoTe$_2$/BTO/LSMO heterostructures.

In addition, we obtained the vertical carrier transport behavior of MoTe$_2$/BTO/LSMO and BTO/LSMO heterostructures by measuring the vertical I–V curves and analyzing the conduction mechanisms (Figure 4b−d and Section S9). The inset in Figure 4b−d schematically depicts the conductive atomic force microscope (CAFM) measurements where the SPM probe is grounded, and the bias is applied to the bottom LSMO electrode, opposite to the PFM and KPFM tests. Therefore, the positive (negative) bias here will switch the polarization of the BTO film to the P_{up} (P_{down}) state. Figure 4b is the vertical I–V curve measured through the MoTe$_2$/BTO/LSMO heterostructure under a small voltage range of ±200

mV. Compared to Figure 4a, a linear $I-V$ relation persists, while the resistance is distinctly increased to 1 MΩ due to the existence of the insulating BTO film. The nonzero current at a small voltage indicates that BTO film possesses some intrinsic free carrier that can be thermally excited. When the voltage range is expanded to ±2 V (Figure 4c), the $I-V$ curve exhibits a nonlinear shape, and its conduction mechanism can be analyzed by fitting the $I-V$ relation according to the expression of different conduction processes. Ohmic conduction, space-charge-limited conduction (SCLC), Schottky emission, Frenkel−Poole (F−P) emission, and Fowler−Nordheim (F−N) tunneling are considered in this work, and the specific analysis process is performed in Section S9. The $I-V$ curve in Figure 4c can be divided into six sections according to different conduction processes. Under positive bias, the current initially follows ohmic conduction under a small electric field, followed by dominant Schottky emission and trap-assisted F−P emission (fitting details in Figure S11). In the negative bias range, the conduction mechanisms are similar to that in the positive bias range, except that SCLC dominates the current conduction in the bias range of −0.71 to −1.26 V (fitting details in Figure S12). This phenomenon follows the feature of strong effective E_{bi} as explained in Figure 1d in comparison with the situation under the P_{up} state (Figure 1e). Meanwhile, the mechanism of F−P emission indicates that many trap states are in the band gap of BTO film and can be activated under a strong electric field. Those in-gap trap states not only lead to vertical conduction under large electric bias but also significantly influence the photoelectric behavior of the MoTe$_2$/BTO/LSMO heterostructure.

In general, a low resistance state was observed under positive bias, and a high resistance state was observed under negative bias (Figure 4c). Compared with holes, electrons are more likely to transport through heterostructure layers because the barrier height in the conduction band (ΔE_c) is significantly lowered than that in the valence band (ΔE_v) (Figure 1d,e). When positive bias is applied to the LSMO film, electrons transport from the MoTe$_2$ film to the LSMO film, and the barrier height at the MoTe$_2$/BTO interface (ΔE_c in Figure 1d) is relatively low to overcome. However, the electrons need to overcome a higher barrier height at the BTO/LSMO interface ($e\Phi_{bo}$ in Figure 1e) to transport under a negative applied bias. This asymmetric potential barrier results in the asymmetric conductive behavior.

To clarify the role of MoTe$_2$ in the heterostructure conduction, we also measured vertical $I-V$ curves of the bare BTO/LSMO, where the Pt-coated SPM probe serves as the top electrode (Figure 4d). The curve exhibits a rectification behavior and the low resistance state is obtained under negative bias. The measured current is much smaller than that obtained from the MoTe$_2$/BTO/LSMO heterostructure. From the conduction mechanism analysis presented in Figure S13, we inferred that Schottky emissions, F−P emissions, and F−N tunneling may all contribute. In the Pt/BTO/LSMO heterostructure, a larger and opposite barrier height asymmetry presents under positive and negative biases, leading to a classic rectification behavior. Therefore, MoTe$_2$ improves the overall conductivity of the heterostructure significantly through appropriate band alignment with BTO.

In the MoTe$_2$/BTO/LSMO heterostructures described above, we observed UV light-induced polarization switching from P_{down} to P_{up} with about 5−8 nm thickness of MoTe$_2$, and conversely from P_{up} to P_{down} with 2.15 nm MoTe$_2$. The PFM

hysteresis loops of the two types of heterostructures (Figures 2c and 3c) demonstrated an opposite imprint direction and amplitude asymmetry, which manifested inversed effective E_{bi} and varied screening charge density in the corresponding heterostructure. Such a discrepancy may be attributed to the change in the band structure of MoTe$_2$ with film thickness. Thus, we conducted KPFM tests of pristine 3-ML MoTe$_2$/BTO and 12-ML MoTe$_2$/BTO heterostructures (Figure S14 and Figure 5a). The obtained surface potential (V_{sp}) is defined as $(\phi_{tip} - \phi_{sample})/e$, where ϕ_{tip} and ϕ_{sample} are work functions of the SPM tip and sample, respectively, and e is the electronic charge. Therefore, the work function has the relation of $\phi_{3L\text{-}MoTe2} > \phi_{BTO} > \phi_{12L\text{-}MoTe2}$ based on the KPFM data, and an opposite direction of charge transfer and reversed band alignments can occur at the 3-ML and 12-ML MoTe$_2$ with the BTO interface, respectively. We also verified the work function of 3-ML and 12-ML MoTe$_2$ by first-principles calculations, and an increased work function has been obtained with the reduction of MoTe$_2$ thickness, in accordance with the KPFM results (Figure 5b,c). Therefore, an inverse contact field and different carrier concentration states occur at the 3-ML MoTe$_2$/BTO and 12-ML MoTe$_2$/BTO interfaces, leading to the opposite UV-induced polarization switching behavior when the thickness of MoTe$_2$ is thinned from 12 to 3 ML. In addition, some works[40,41] indicated that MoTe$_2$ is sensitive to hydrogen and oxygen adsorptions due to its intrinsic Te defects, especially for monolayer MoTe$_2$. Therefore, 3-ML MoTe$_2$ may also adsorb polar molecules and cause extra doping of the MoTe$_2$ film. As discussed earlier, when the polarization field aligns with the contact field, the effective E_{bi} will be increased and massive carriers can be accumulated at the MoTe$_2$/BTO interface. Simulations using COMSOL Multiphysics were conducted to calculate the carrier concentrations at the MoTe$_2$/BTO interface after applying a positive or negative bias, the geometrical model of which is shown in Figure S15a. As depicted in Figure 5d,e, only electrons are gathered at the 3-ML MoTe$_2$/BTO interface when −5 V_{dc} bias was applied to switch the polarization of BTO to the P_{up} state, and more holes are accumulated at the 12-ML MoTe$_2$/BTO interface under +5 V_{dc} bias (BTO in the P_{down} state). These massive space charges offer enhanced effective E_{bi} to facilitate the transferring of the photoinduced carriers after UV illumination, thus switching the polarity of screening charges and the polarization direction of BTO film. The schematics of the band structure under UV light are shown in Figure 5f,g. Under UV light illumination, carriers in both MoTe$_2$ and BTO films can be excited and transferred under E_{bi1} and E_{bi2}. The possible in-gap states in the MoTe$_2$ and BTO film (manifested by a gray cycle with a line in Figure 5f,g) probably trap some photoinduced carriers and decelerate the process of UV light-induced polarization switching. In general, E_{bi} in ferroelectric heterostructures is an effective field involving multiple effects, including the contact field, polarization field, screening conditions,[42] and interface pinning effects.

On the contrary, if the polarization field is in the opposite direction to the contact field, the effective E_{bi} will be reduced and even be switched to the reversed direction. In Figure S15b, although more holes are gathered at the 3-ML MoTe$_2$/BTO (P_{down} state by +5 V_{dc} bias) interface, the carrier concentration difference is lower than that at the 3-ML MoTe$_2$/BTO (P_{up} state by −5 V_{dc} bias) interface. Therefore, the enhanced effective E_{bi} is still obtained when a +5 V bias is applied. For

the 12-ML MoTe$_2$/BTO heterostructure, the opposite effect applies (Figure S16a). The space charges generated weakened the effective E_{bi}, and only a few photoinduced holes of MoTe$_2$ and BTO films are transferred to the MoTe$_2$/BTO interface, which cannot compensate the existing polarization charge and thus cannot switch the polarity of BTO polarization. Therefore, no UV-induced polarization switching behavior under this type of heterostructure was observed, as shown in Figures S15c and S16b. In summary, the overall band diagrams under UV illumination, including 3-ML MoTe$_2$/BTO(P_{down})/LSMO, 3-ML MoTe$_2$/BTO(P_{up})/LSMO, 12-ML MoTe$_2$/BTO(P_{down})/LSMO, and 12-ML MoTe$_2$/BTO(P_{up})/LSMO are demonstrated in Figure S17 to explicitly manifest the mechanism of UV light-induced polarization switching behavior.

3. CONCLUSIONS

In this work, we fabricated MoTe$_2$/BTO/LSMO heterostructures and conducted a comprehensive investigation into their electrically induced and optically induced polarization switching behavior, as well as the electric transport behaviors. We observed that UV light was capable of inducing polarization switching from P_{down} to P_{up} states with thicker MoTe$_2$ (around 5−8 nm) in the heterostructure, and conversely from P_{up} to P_{down} states with thinner MoTe$_2$ (around 2 nm). We attribute these behaviors to the thickness-dependent band structure of MoTe$_2$ films, which generates an opposite contact field upon the formation of MoTe$_2$/BTO/LSMO heterostructures. This is further supported by the imprint behavior observed in PFM hysteresis loops, the work function calculations by DFT, and the interface carrier concentration calculated by COMSOL Multiphysics simulation. When the polarization field of BTO is aligned with the contact field, enhanced effective E_{bi} was observed, motivating the transfer of UV-induced carriers in both MoTe$_2$ and BTO films. This facilitated the switching of the polarization orientation of BTO film by changing the type of interfacial charges. The coherent modulation of the effective E_{bi} by the contact field, polarization field, and optically excited carriers was identified as the key factor for the observed UV-induced polarization switching in the heterostructure. Furthermore, electric transport measurements of the MoTe$_2$/BTO/LSMO heterostructures revealed the magnitude of the interface barrier height and E_{bi} under different polarization states of BTO (P_{up} or P_{down}). We also verified the presence of numerous in-gap trap states inherently in MoTe$_2$ and BTO films, which can have the effect of decelerating the process of UV-induced polarization switching. The observations in this work provide an advancement in the development of multifield modulation of ferroelectric polarization, and pave the way for potential applications based on the heterostructures formed by 2D materials and ferroelectric thin films in the field of nanoelectronic and optoelectronic devices.

4. EXPERIMENTAL SECTION

4.1. Preparation of MoTe$_2$/BaTiO$_3$/La$_{0.7}$Sr$_{0.3}$MnO$_3$ Heterostructures. The BTO/LSMO films were grown epitaxially on SrTiO$_3$(STO) by pulsed laser deposition (PLD) using a XeCl excimer laser (λ = 308 nm) with a fluence of 1.75 J cm^{-2} and a repetition rate of 2 Hz. The thickness of the BTO layer is 36 u.c. (about 15 nm). The MoTe$_2$ layer with a thickness spanning from 2 to 8 nm was prepared by mechanical exfoliation method from a 2H-MoTe$_2$ single crystal. The MoTe$_2$ film was first exfoliated using

commercial PDMS and then transferred to the target substrate BTO/LSMO/STO using a mechanical transfer platform. To ensure interface cleanliness, the heterostructure was prepared under an N$_2$ atmosphere, and the substrate BTO/LSMO/STO was cleaned first.

4.2. Crystal Structure Measurement. The crystal structures of the BTO/LSMO/STO substrate and 2H-MoTe$_2$ single crystal were characterized by X-ray diffraction and photoluminescence spectrometry. X-ray diffraction was tested on Bruker D8 Advance equipment with the parameters of 40 kV, 40 mA, and Cu target K$_\alpha$1 radiation. Photoluminescence spectrometry was carried out on an FLSPP20 steady state and lifetime fluorescence spectrometer with 270 nm excitation wavelength. Due to the similar binding energy between 2H-MoTe$_2$ and 1T′-MoTe$_2$, the Raman spectrum of MoTe$_2$/BTO/LSMO heterostructure was measured to ensure the phase of the MoTe$_2$ film, and the wavelength of excitation light was 532 nm.

4.3. PFM Measurements. The ferroelectric domain structures were obtained by using a commercial scanning probe microscopy system (MFP-3D, Oxford Instruments, USA). The dual AC resonance tracking piezoresponse force microscopy (DART-PFM) technique was used to track the contact resonance frequency in real-time and maintain a high signal-to-noise ratio in PFM images. A conductive probe with a nanoscale sharp tip (PPP-EFM, NANOSENSORS, Switzerland, with a Pt coating and around 25 nm tip radius) was in contact with the surface of the sample while applying an AC bias during the scan. According to the inverse piezoelectric effect, mechanical oscillation of the piezoelectric material was induced and detected by the probe as well. In PFM measurements, the amplitude signal indicates the strength of the piezoresponse, which is proportional to the piezoelectric constant, and the phase signal provides information on relative polarization orientations. PFM can also perform switching spectroscopy mode in which the amplitude loop and phase loop manifest the local polarization switching process under a DC bias sweep.

4.4. KPFM Measurements. Kelvin probe force microscopy (KPFM) is the technique to obtain the surface potential or work function of materials via a dual-pass method. In this work, during the first pass, surface morphology was required, whereas, in the second pass, an AC bias was applied to a conductive tip to produce an electrostatic force between the tip and sample while maintaining a constant separation (∼40 nm) between them. Meanwhile, a DC bias was applied to the conductive tip to null the first-order component of the tip−sample interaction force. In this case, the DC bias equaled the potential difference between the tip and sample and gave the relative surface potential distribution of materials.

4.5. CAFM Measurements. Conductive atomic force microscopy (CAFM) is a technique to measure the local conductivity of a sample based on contact mode, and both surface current mapping and vertical current−voltage curves can be obtained. In the CAFM test used in this work, the probe tip was grounded and a bias was imposed on the bottom electrode of the sample to form a vertical electrical field. To maintain good contact and low contact resistance between the probe and sample, it is critical to exert a suitable loading force on the probe (about 250 nN in this case).

4.6. Device Fabrication and Electrical Measurements of MoTe$_2$ Film. To acquire the lateral conductivity of MoTe$_2$ film in this research, we fabricated two 50 nm Au/5 nm Ti electrodes on the surface of MoTe$_2$/BTO/LSMO heterostructure as the source and drain electrodes. The electrodes were fabricated by the process of ultraviolet lithography and ultrahigh vacuum electron beam deposition. Keithley 4200 semiconductor characterization system combined with a probe station was used to measure the lateral current−voltage (I_{ds}−V_{ds}) curves of MoTe$_2$ film when 0 V gate bias was applied on the LSMO bottom electrode.

4.7. In Situ Photoelectric SPM Measurements. A commercial scanning probe microscopy system (MFP-3D, Oxford Instruments, USA) equipped with an open modular optical design was used to provide bottom-side sample illumination. The optical path can adjust the focus of light illuminating a sample and can easily accommodate external light sources. In this case, a stabilized deuterium UV light source (SL S204, Thorlabs Inc., a strong and continuous light at the

wavelength of 200−400 nm for UV illumination) and xenon broadband light source (7ILX500, SOFN Instruments Co. Ltd., for 450 nm illumination) were used to motivate the photoelectric coupling effect of MoTe$_2$/BTO/LSMO heterostructures. A double grating scanning spectrometer (7ISW151, SOFN Instruments Co. Ltd.) was coupled with a xenon broadband light source to obtain a monochromatic light with an accurate 450 nm wavelength. The power density of UV light illuminated on the surface of the heterostructure is 4.96 mW cm^{-2}, and that of 450 nm light applied on the surface of the sample is 3.37 mW cm^{-2}. In situ PFM and KPFM tests can be achieved when light is shined on the sample.

4.8. First-Principles Calculation. First-principles calculations were carried out within the DFT formalism, as implemented in the Vienna ab initio simulation package (VASP).[43] The Perdew−Burke−Ernzerhof (PBE)[44] realization of the generalized gradient approximation (GGA) was used for the exchange−correlation functional with a projector augmented-wave (PAW)[45] pseudopotentials, treating the Mo 4p 5s 4d and Te 5s 5p as valence electrons. The projector-augmented wave method was employed to model the ionic potentials. The energy cutoff was set to 400 eV for all calculations. A vacuum space of 60 Å was introduced to avoid interactions between the image structures. The Grimme's method (DFT-D3)[46] van der Waals correction was adopted. All the atoms are allowed to relax until the calculated forces are less than 0.01 eV Å^{-1}, while the electronic minimization was applied with a tolerance of 10^{-5} eV. The Monkhorst-pack k-point[47] sampling was used for the Brillouin zone integration: 15 × 15 × 1 for relaxation and self-consistent calculations.

4.9. COMSOL Multiphysics Simulation. The three-dimensional carrier distribution of the MoTe$_2$/BTO heterostructure is modeled using the static transport equation in the semiconductor module of COMSOL Multiphysics simulation, and the geometrical model is shown in Figure S14a. A pyramid conductive tip (Pt coating) contacts the surface of the MoTe$_2$ layer, and the LSMO bottom electrode is set beneath the BTO layer. An external bias V_{dc} was applied on the tip, and the bias of the LSMO layer was always set as 0 V. A continuous quasi-Fermi level model is used at the MoTe$_2$/BTO interface, and the interfaces of tip/MoTe$_2$ and BTO/LSMO are installed as an ideal Schottky semiconductor-metal contact. An insulation boundary condition was imposed on all other interfaces. All of the simulation parameters are performed in Table S2.

■ ASSOCIATED CONTENT

Data Availability Statement

The data that support the findings of this study are available from the corresponding author upon reasonable request.

Ⓢ Supporting Information

The Supporting Information is available free of charge at https://pubs.acs.org/doi/10.1021/acsami.3c18179.

> Hysteresis loops of MoTe$_2$/BTO/LSMO and BTO/LSMO heterostructures, band alignment of MoTe$_2$ (12-ML)/BTO/LSMO heterostructure, crystal structure and band gap of MoTe$_2$ crystal and BTO film, Raman spectrum of MoTe$_2$/BTO/LSMO heterostructure, polarization switching behavior induced by 450 nm light illumination, polarization switching process of MoTe$_2$/BTO/LSMO heterostructure under different UV illumination durations, switching characteristics of other MoTe$_2$/BTO/LSMO heterostructure under UV illumination, band structure of MoTe$_2$ (3-ML)/BTO/LSMO heterostructure, conductive mechanism of MoTe$_2$/BTO/LSMO and BTO/LSMO heterostructures, and mechanisms of UV light-induced polarization switching behavior of MoTe$_2$/BTO/LSMO heterostructures (PDF)

■ AUTHOR INFORMATION

Corresponding Authors

Kaiyang Zeng − Department of Mechanical Engineering, National University of Singapore, Singapore 117576, Singapore; ⓞ orcid.org/0000-0002-3348-0018; Email: mpezk@nus.edu.sg

Tao Li − Center for Spintronics and Quantum Systems, State Key Laboratory for Mechanical Behavior of Materials, Department of Materials Science and Engineering, Xi'an Jiaotong University, Xi'an 710049, China; ⓞ orcid.org/0009-0008-6820-3863; Email: taoli66@xjtu.edu.cn

Authors

Yuqing Zhou − Center for Spintronics and Quantum Systems, State Key Laboratory for Mechanical Behavior of Materials, Department of Materials Science and Engineering, Xi'an Jiaotong University, Xi'an 710049, China; Department of Mechanical Engineering, National University of Singapore, Singapore 117576, Singapore; ⓞ orcid.org/0000-0001-7986-5338

Chao Yang − Center for Spintronics and Quantum Systems, State Key Laboratory for Mechanical Behavior of Materials, Department of Materials Science and Engineering, Xi'an Jiaotong University, Xi'an 710049, China

Xingke Fu − Beijing National Laboratory for Condensed Matter Physics, Institute of Physics, Chinese Academy of Sciences, Beijing 100190, China

Yadong Liu − Center for Spintronics and Quantum Systems, State Key Laboratory for Mechanical Behavior of Materials, Department of Materials Science and Engineering, Xi'an Jiaotong University, Xi'an 710049, China

Yulin Yang − Center for Spintronics and Quantum Systems, State Key Laboratory for Mechanical Behavior of Materials, Department of Materials Science and Engineering, Xi'an Jiaotong University, Xi'an 710049, China

Yongyi Wu − Center for Spintronics and Quantum Systems, State Key Laboratory for Mechanical Behavior of Materials, Department of Materials Science and Engineering, Xi'an Jiaotong University, Xi'an 710049, China

Chen Ge − Beijing National Laboratory for Condensed Matter Physics, Institute of Physics, Chinese Academy of Sciences, Beijing 100190, China; ⓞ orcid.org/0000-0002-8093-940X

Tai Min − Center for Spintronics and Quantum Systems, State Key Laboratory for Mechanical Behavior of Materials, Department of Materials Science and Engineering, Xi'an Jiaotong University, Xi'an 710049, China

Complete contact information is available at:
https://pubs.acs.org/10.1021/acsami.3c18179

Notes

The authors declare no competing financial interest.

■ REFERENCES

(1) Očenášek, J.; Lu, H.; Bark, C. W.; Eom, C. B.; Alcalá, J.; Catalan, G.; Gruverman, A. Nanomechanics of Flexoelectric Switching. *Phys. Rev. B* **2015**, *92*, No. 035417.

(2) Dong, G.; Li, S.; Li, T.; Wu, H.; Nan, T.; Wang, X.; Liu, H.; Cheng, Y.; Zhou, Y.; Qu, W.; Zhao, Y.; Peng, B.; Wang, Z.; Hu, Z.; Luo, Z.; Ren, W.; Pennycook, S. J.; Li, J.; Sun, J.; Ye, Z.; Jiang, Z.; Zhou, Z.; Ding, X.; Min, T.; Liu, M. Periodic Wrinkle-Patterned Single-Crystalline Ferroelectric Oxide Membranes with Enhanced Piezoelectricity. *Adv. Mater.* **2020**, *32*, 2004477.

(3) Zhou, Y.; Guo, C.; Dong, G.; Liu, H.; Zhou, Z.; Niu, B.; Wu, D.; Li, T.; Huang, H.; Liu, M.; Min, T. Tip-Induced in-Plane Ferroelectric Superstructure in Zigzag-Wrinkled $BaTiO_3$ Thin Films. *Nano Lett.* **2022**, *22*, 2859−2866.

(4) Gómez, A.; Vila-Fungueiriño, J. M.; Moalla, R.; Saint-Girons, G.; Gázquez, J.; Varela, M.; Bachelet, R.; Gich, M.; Rivadulla, F.; Carretero-Genevrier, A. Electric and Mechanical Switching of Ferroelectric and Resistive States in Semiconducting $BaTiO_{3−δ}$ Films on Silicon. *Small* **2017**, *13*, 1701614.

(5) Zhang, F.; Fan, H.; Han, B.; Zhu, Y.; Deng, X.; Edwards, D.; Kumar, A.; Chen, D.; Gao, X.; Fan, Z.; Rodriguez, B. J. Boosting Polarization Switching-Induced Current Injection by Mechanical Force in Ferroelectric Thin Films. *ACS Appl. Mater. Interfaces* **2021**, *13*, 26180−26186.

(6) Wang, R. V.; Fong, D. D.; Jiang, F.; Highland, M. J.; Fuoss, P. H.; Thompson, C.; Kolpak, A. M.; Eastman, J. A.; Streiffer, S. K.; Rappe, A. M.; Stephenson, G. B. Reversible Chemical Switching of a Ferroelectric Film. *Phys. Rev. Lett.* **2009**, *102*, No. 047601.

(7) Thong, H.; Li, Z.; Lu, J.; Li, C.; Liu, Y.; Sun, Q.; Fu, Z.; Wei, Y.; Wang, K. Domain Engineering in Bulk Ferroelectric Ceramics Via Mesoscopic Chemical Inhomogeneity. *Adv. Sci.* **2022**, *9*, 2200998.

(8) Li, T.; Lipatov, A.; Lu, H.; Lee, H.; Lee, J. W.; Torun, E.; Wirtz, L.; Eom, C. B.; Íñiguez, J.; Sinitskii, A.; Gruverman, A. Optical Control of Polarization in Ferroelectric Heterostructures. *Nat. Commun.* **2018**, *9*, 3344.

(9) Li, D.; Huang, X.; Wu, Q.; Zhang, L.; Lu, Y.; Hong, X. Ferroelectric Domain Control of Nonlinear Light Polarization in MoS_2 Via $PbZr_{0.2}Ti_{0.8}O_3$ Thin Films and Free-Standing Membranes. *Adv. Mater.* **2023**, *35*, 2208825.

(10) Liu, F.; Fina, I.; Sauthier, G.; Sánchez, F.; Rappe, A. M.; Fontcuberta, J. Control of the Polarization of Ferroelectric Capacitors by the Concurrent Action of Light and Adsorbates. *ACS Appl. Mater. Interfaces* **2018**, *10*, 23968−23975.

(11) Steigerwald, H.; Ying, Y. J.; Eason, R. W.; Buse, K.; Mailis, S.; Soergel, E. Direct Writing of Ferroelectric Domains on the X- and Y-Faces of Lithium Niobate Using a Continuous Wave Ultraviolet Laser. *Appl. Phys. Lett.* **2011**, *98*, No. 062902.

(12) Boes, A.; Crasto, T.; Steigerwald, H.; Wade, S.; Frohnhaus, J.; Soergel, E.; Mitchell, A. Direct Writing of Ferroelectric Domains on Strontium Barium Niobate Crystals Using Focused Ultraviolet Laser Light. *Appl. Phys. Lett.* **2013**, *103*, 142904.

(13) Yang, M.; Alexe, M. Light-Induced Reversible Control of Ferroelectric Polarization in $BiFeO_3$. *Adv. Mater.* **2018**, *30*, 1704908.

(14) Luo, Z. D.; Park, D. S.; Yang, M. M.; Alexe, M. Light-Controlled Nanoscopic Writing of Electronic Memories Using the Tip-Enhanced Bulk Photovoltaic Effect. *ACS Appl. Mater. Interfaces* **2019**, *11*, 8276−8283.

(15) Lipatov, A.; Vorobeva, N. S.; Li, T.; Gruverman, A.; Sinitskii, A. Using Light for Better Programming of Ferroelectric Devices: Optoelectronic MoS_2-Pb(Zr,Ti)O_3 Memories with Improved On−Off Ratios. *Adv. Electron. Mater.* **2021**, *7*, 2001223.

(16) Du, J.; Xie, D.; Zhang, Q.; Zhong, H.; Meng, F.; Fu, X.; Sun, Q.; Ni, H.; Li, T.; Guo, E. J.; Guo, H.; He, M.; Wang, C.; Gu, L.; Xu, X.; Zhang, G.; Yang, G.; Jin, K.; Ge, C. A Robust Neuromorphic Vision Sensor with Optical Control of Ferroelectric Switching. *Nano Energy* **2021**, *89*, No. 106439.

(17) Long, X.; Tan, H.; Sánchez, F.; Fina, I.; Fontcuberta, J. Non-Volatile Optical Switch of Resistance in Photoferroelectric Tunnel Junctions. *Nat. Commun.* **2021**, *12*, 382.

(18) Tan, H.; Castro, G.; Lyu, J.; Loza-Alvarez, P.; Sánchez, F.; Fontcuberta, J.; Fina, I. Control of up-to-Down/Down-to-up Light-Induced Ferroelectric Polarization Reversal. *Materials Horizons* **2022**, *9*, 2345−2352.

(19) Lee, D.; Baek, S. H.; Kim, T. H.; Yoon, J. G.; Folkman, C. M.; Eom, C. B.; Noh, T. W. Polarity Control of Carrier Injection at Ferroelectric/Metal Interfaces for Electrically Switchable Diode and Photovoltaic Effects. *Phys. Rev. B* **2011**, *84*, No. 125305.

(20) Furchi, M. M.; Pospischil, A.; Libisch, F.; Burgdörfer, J.; Mueller, T. Photovoltaic Effect in an Electrically Tunable Van Der Waals Heterojunction. *Nano Lett.* **2014**, *14*, 4785−4791.

(21) Akamatsu, T.; Ideue, T.; Zhou, L.; Dong, Y.; Kitamura, S.; Yoshii, M.; Yang, D.; Onga, M.; Nakagawa, Y.; Watanabe, K.; Taniguchi, T.; Laurienzo, J.; Huang, J.; Ye, Z.; Morimoto, T.; Yuan, H.; Iwasa, Y. A Van Der Waals Interface That Creates in-Plane Polarization and a Spontaneous Photovoltaic Effect. *Science* **2021**, *372*, 68−72.

(22) Lipatov, A.; Sharma, P.; Gruverman, A.; Sinitskii, A. Optoelectrical Molybdenum Disulfide (MoS_2)—Ferroelectric Memories. *ACS Nano* **2015**, *9*, 8089−8098.

(23) Ghasemi, P.; Sharifi, M. J. Optoelectronic Memory Capacitor Based on Manipulation of Ferroelectric Properties. *ACS Appl. Mater. Interfaces* **2021**, *13*, 53067−53072.

(24) Kundys, D.; Cascales, A.; Makhort, A. S.; Majjad, H.; Chevrier, F.; Doudin, B.; Fedrizzi, A.; Kundys, B. Optically Rewritable Memory in a Graphene-Ferroelectric-Photovoltaic Heterostructure. *Phys. Rev. Appl.* **2020**, *13*, No. 064034.

(25) Guo, R.; You, L.; Zhou, Y.; Shiuh Lim, Z.; Zou, X.; Chen, L.; Ramesh, R.; Wang, J. Non-Volatile Memory Based on the Ferroelectric Photovoltaic Effect. *Nat. Commun.* **2013**, *4*, 1990.

(26) Zheng, D.; Dong, X.; Lu, J.; Niu, Y.; Wang, H. High-Sensitivity Infrared Photoelectric Detection Based on Ws2/Si Structure Tuned by Ferroelectrics. *Small* **2022**, *18*, 2105188.

(27) Indiveri, G.; Douglas, R. Neuromorphic Vision Sensors. *Science* **2000**, *288*, 1189−1190.

(28) Luo, Z. D.; Xia, X.; Yang, M. M.; Wilson, N. R.; Gruverman, A.; Alexe, M. Artificial Optoelectronic Synapses Based on Ferroelectric Field-Effect Enabled 2D Transition Metal Dichalcogenide Memristive Transistors. *ACS Nano* **2020**, *14*, 746−754.

(29) Sun, C.; Wade, M. T.; Lee, Y.; Orcutt, J. S.; Alloatti, L.; Georgas, M. S.; Waterman, A. S.; Shainline, J. M.; Avizienis, R. R.; Lin, S.; Moss, B. R.; Kumar, R.; Pavanello, F.; Atabaki, A. H.; Cook, H. M.; Ou, A. J.; Leu, J. C.; Chen, Y.-H.; Asanović, K.; Ram, R. J.; Popović, M. A.; Stojanović, V. M. Single-Chip Microprocessor That Communicates Directly Using Light. *Nature* **2015**, *528*, 534−538.

(30) Tong, L.; Peng, Z.; Lin, R.; Li, Z.; Wang, Y.; Huang, X.; Xue, K. H.; Xu, H.; Liu, F.; Xia, H.; Wang, P.; Xu, M.; Xiong, W.; Hu, W.; Xu, J.; Zhang, X.; Ye, L.; Miao, X. 2d Materials-based Homogeneous Transistor-Memory Architecture for Neuromorphic Hardware. *Science* **2021**, *373*, 1353−1358.

(31) Wang, X.; Zhu, C.; Deng, Y.; Duan, R.; Chen, J.; Zeng, Q.; Zhou, J.; Fu, Q.; You, L.; Liu, S.; Edgar, J. H.; Yu, P.; Liu, Z. Van Der Waals Engineering of Ferroelectric Heterostructures for Long-Retention Memory. *Nat. Commun.* **2021**, *12*, 1109.

(32) Wen, Z.; Wu, D. Ferroelectric Tunnel Junctions: Modulations on the Potential Barrier. *Adv. Mater.* **2020**, *32*, 1904123.

(33) Li, P.; Chaturvedi, A.; Zhou, H.; Zhang, G.; Li, Q.; Xue, J.; Zhou, Z.; Wang, S.; Zhou, K.; Weng, Y.; Zheng, F.; Shi, Z.; Teo, E. H. T.; Fang, L.; You, L. Electrostatic Coupling in MoS_2/CuInP$_2$S$_6$ Ferroelectric Vdw Heterostructures. *Adv. Funct. Mater.* **2022**, *32*, 2201359.

(34) Wu, G.; Tian, B.; Liu, L.; Lv, W.; Wu, S.; Wang, X.; Chen, Y.; Li, J.; Wang, Z.; Wu, S.; Shen, H.; Lin, T.; Zhou, P.; Liu, Q.; Duan, C.; Zhang, S.; Meng, X.; Wu, S.; Hu, W.; Wang, X.; Chu, J.; Wang, J. Programmable Transition Metal Dichalcogenide Homojunctions Controlled by Nonvolatile Ferroelectric Domains. *Nature Electronics* **2020**, *3*, 43−50.

(35) Li, Y.; Yang, M.; Lu, Y.; Cao, D.; Chen, X.; Shu, H. Reversible Doping Polarity and Ultrahigh Carrier Density in Two-Dimensional

Van Der Waals Ferroelectric Heterostructures. *Front. Phys.* **2023**, *18*, 33307.

(36) Ghimire, M. K.; Ji, H.; Gul, H. Z.; Yi, H.; Jiang, J.; Lim, S. C. Defect-Affected Photocurrent in $MoTe_2$ Fets. *ACS Appl. Mater. Interfaces* **2019**, *11*, 10068−10073.

(37) Lezama, I. G.; Ubaldini, A.; Longobardi, M.; Giannini, E.; Renner, C.; Kuzmenko, A. B.; Morpurgo, A. F. Surface Transport and Band Gap Structure of Exfoliated $2H$-$MoTe_2$ Crystals. *2D Materials* **2014**, *1*, No. 021002.

(38) Lin, Y.; Xu, Y.; Wang, S.; Li, S.; Yamamoto, M.; Aparecido-Ferreira, A.; Li, W.; Sun, H.; Nakaharai, S.; Jian, W.; Ueno, K.; Tsukagoshi, K. Ambipolar $MoTe_2$ Transistors and Their Applications in Logic Circuits. *Adv. Mater.* **2014**, *26*, 3263−3269.

(39) Zhu, H.; Wang, Q.; Cheng, L.; Addou, R.; Kim, J.; Kim, M. J.; Wallace, R. M. Defects and Surface Structural Stability of $MoTe_2$ under Vacuum Annealing. *ACS Nano* **2017**, *11*, 11005−11014.

(40) Liu, X.; Islam, A.; Guo, J.; Feng, P. X. L. Controlling Polarity of Mote2 Transistors for Monolithic Complementary Logic Via Schottky Contact Engineering. *ACS Nano* **2020**, *14*, 1457−1467.

(41) Ruppert, C.; Aslan, B.; Heinz, T. F. Optical Properties and Band Gap of Single- and Few-Layer $MoTe_2$ Crystals. *Nano Lett.* **2014**, *14*, 6231−6236.

(42) Wurfel, P.; Batra, I. P. Depolarization-Field-Induced Instability in Thin Ferroelectric Films—Experiment and Theory. *Phys. Rev. B* **1973**, *8*, 5126−5133.

(43) Kresse, G.; Furthmüller, J. Efficient Iterative Schemes for Ab Initio Total-Energy Calculations Using a Plane-Wave Basis Set. *Phys. Rev. B* **1996**, *54*, 11169−11186.

(44) Perdew, J. P.; Burke, K.; Ernzerhof, M. Generalized Gradient Approximation Made Simple. *Phys. Rev. Lett.* **1996**, *77*, 3865−3868.

(45) Blöchl, P. E. Projector Augmented-Wave Method. *Phys. Rev. B* **1994**, *50*, 17953−17979.

(46) Grimme, S.; Ehrlich, S.; Goerigk, L. Effect of the Damping Function in Dispersion Corrected Density Functional Theory. *J. Comput. Chem.* **2011**, *32*, 1456−1465.

(47) Monkhorst, H. J.; Pack, J. D. Special Points for Brillouin-Zone Integrations. *Phys. Rev. B* **1976**, *13*, 5188−5192.